



**HAL**  
open science

# Effect of porosity on effective diagonal stiffness coefficients (cii) and elastic anisotropy of cortical bone at 1MHz: A finite-difference time domain study

Cécile Baron, Maryline Talmant, Pascal Laugier

## ► To cite this version:

Cécile Baron, Maryline Talmant, Pascal Laugier. Effect of porosity on effective diagonal stiffness coefficients (cii) and elastic anisotropy of cortical bone at 1MHz: A finite-difference time domain study. *Journal of the Acoustical Society of America*, 2007, 122, pp.1810 - 1817. 10.1121/1.2759165 . hal-04444913

**HAL Id: hal-04444913**

**<https://hal.science/hal-04444913>**

Submitted on 7 Feb 2024

**HAL** is a multi-disciplinary open access archive for the deposit and dissemination of scientific research documents, whether they are published or not. The documents may come from teaching and research institutions in France or abroad, or from public or private research centers.

L'archive ouverte pluridisciplinaire **HAL**, est destinée au dépôt et à la diffusion de documents scientifiques de niveau recherche, publiés ou non, émanant des établissements d'enseignement et de recherche français ou étrangers, des laboratoires publics ou privés.

# 1 Effect of porosity on effective diagonal stiffness coefficients ( $c_{ii}$ ) 2 and elastic anisotropy of cortical bone at 1 MHz: A finite- 3 difference time domain study

4 Cécile Baron,<sup>a)</sup> Maryline Talmant, and Pascal Laugier  
5 *Université Pierre et Marie Curie-Paris 6, Laboratoire d'Imagerie Paramétrique, Paris F-75005, France*  
6 *and CNRS, LIP, Paris F- 75006, France*

7 (Received 16 March 2007; revised 12 June 2007; accepted 21 June 2007)

8 Finite-difference time domain (FDTD) numerical simulations coupled to real experimental data  
9 were used to investigate the propagation of 1 MHz pure bulk wave propagation through models of  
10 cortical bone microstructures. Bone microstructures were reconstructed from three-dimensional  
11 high resolution synchrotron radiation microcomputed tomography (SR- $\mu$ CT) data sets. Because the  
12 bone matrix elastic properties were incompletely documented, several assumptions were made. Four  
13 built-in bone matrix models characterized by four different anisotropy ratios but the same Poisson's  
14 ratios were tested. Combining them with the reconstructed microstructures in the FDTD  
15 computations, effective stiffness coefficients were derived from simulated bulk-wave velocity  
16 measurements. For all the models, all the effective compression and shear bulk wave velocities were  
17 found to decrease when porosity increases. However, the trend was weaker in the axial direction  
18 compared to the transverse directions, contributing to the increase of the effective anisotropy. On the  
19 other hand, it was shown that the initial Poisson's ratio value may substantially affect the variations  
20 of the effective stiffness coefficients. The present study can be used to elaborate sophisticated  
21 macroscopic computational bone models incorporating realistic CT-based macroscopic bone  
22 structures and effective elastic properties derived from  $\mu$ CT-based FDTD simulations including the  
23 cortical porosity effect. © 2007 Acoustical Society of America. [DOI: 10.1121/1.2759165]

24 PACS number(s): 43.80.Ev, 43.80.Qf, 43.80.Jz, 43.80.Vj [FD]

Pages: 1–XXXX

## 26 I. INTRODUCTION

AQ: 27 Quantitative ultrasound has received considerable inter-  
#1 28 est in recent years for its potential to assess different bone  
29 properties that are relevant to predict bone fragility.

30 Axial transmission is a generic term to designate a vari-  
31 ety of techniques devised to assess cortical bone using a  
32 linear arrangement of ultrasound emitters and receivers  
33 placed on top of the overlying soft tissue. A part of the ul-  
34 trasonic energy is guided along the cortex and can be radi-  
35 ated at the interface between soft tissue and bone. Various  
36 technical implementations of the technique have been pro-  
37 posed at different frequencies in the range 250  
38 kHz–1.25 MHz.<sup>1–4</sup>

39 Several wave types contribute to the total pressure field  
40 sensed by the receivers. The first arriving signal (FAS) is of  
41 special interest for *in vivo* assessment of cortical bone be-  
42 cause it arrives prior to all other contributions, and therefore,  
43 can be easily determined from time-of-flight measurements  
44 of the signals received at different positions parallel to the  
45 interface.<sup>5</sup> The nature of the wave associated with the first  
46 arriving signal was found to change with increasing cortical  
47 thickness to wavelength ratio ( $\text{Cort.Th}/\lambda$ ) from an  $S_0$  Lamb  
48 mode for  $\text{Cort.Th}/\lambda \ll 1$  to a lateral wave for  
49  $\text{Cort.Th}/\lambda \gg 1$ .<sup>6</sup>

50 Recently, axial transmission approaches have been de-  
51 scribed that work in a low frequency range and exploit a later

arriving signal, a slow guided wave mode, in addition to the  
FAS.<sup>4,7,8</sup> This guided wave mode is well described by the  
theory for guided waves in plate [fundamental antisymmetric  
(or flexural) guided wave].<sup>2</sup>

Clinical trials revealed the ability of these techniques in  
discriminating normal and osteoporotic subjects.<sup>1,9,10</sup> Clini-  
cal performances were enlightened by *in vitro* experiments.  
Experimental studies on excised human radii demonstrate the  
sensitivity of FAS velocity to porosity and degree of  
mineralization<sup>5</sup> and also to intrinsic elastic properties.<sup>11</sup> In  
addition, the velocity of the fundamental antisymmetric  
guided wave shows an exquisite sensitivity to cortical  
thickness.<sup>12,13</sup>

Another approach used to give insight into clinical per-  
formances is the modeling of ultrasound propagation in axial  
transmission configuration. Bone finite-difference time do-  
main (FDTD) studies, using either a generic model of the  
structure (plate or tube models)<sup>6,13</sup> or bone structures recon-  
structured from three-dimensional x-ray tomography data, pro-  
vided valuable insights into the relationships between ultra-  
sound propagation characteristics (e.g., velocity of FAS or  
flexural mode) and bone properties such as cortical thickness  
and porosity. However, in these previous works, the models  
ignore the true local material properties, generic values were  
used instead.

We assume that the prediction capabilities of the com-  
puted tomography (CT) based finite-difference simulations  
may be enhanced with further refinements such as incorpo-  
rating in the model individualized material properties.

<sup>a)</sup>Electronic mail: norabelic@yahoo.fr

81 Bone is a poroelastic medium with a porous network  
 82 filled with a fluid-like medium (marrow) embedded in an  
 83 elastic tissue matrix. Cortical porosity mainly consists in an  
 84 oriented network of Haversian canals of typically  $50\ \mu\text{m}$  di-  
 85 ameter approximately aligned with the long axis of the bone  
 86 and of resorption cavities around  $50\text{--}200\ \mu\text{m}$  in diameter. At  
 87 a smaller scale, small transverse canaliculi and osteocytes  
 88 lacunae (typically less than  $10\ \mu\text{m}$  diameter) also contribute  
 89 to cortical porosity. Each Haversian canal is surrounded by a  
 90 layered cylindrical structure, called osteon, of typically  
 91  $200\ \mu\text{m}$  diameter and between the osteons is the highly min-  
 92 eralized interstitial tissue. The wavelength in axial transmis-  
 93 sion is much longer than the typical size of these structures  
 94 and the material properties required as input into the bone  
 95 computational models are effective properties, the values of  
 96 which are determined by the anisotropic elastic properties of  
 97 the bone tissue matrix and by the oriented cortical porosity.  
 98 First, the presence of pores inside the cortex induces a de-  
 99 crease of whole bone stiffness and density compared to stiff-  
 100 ness and density of the bone matrix.<sup>14</sup> Second, due to its  
 101 preferential orientation, the porous network contributes to  
 102 the mechanical anisotropy of bone.<sup>15</sup> Progress in CT-based  
 103 FDTD models requires knowing the effective individual ma-  
 104 terial properties in which the effects of both cortical porosity  
 105 and anisotropic elasticity are properly taken into account.

106 Scarce data on porosity-related anisotropic stiffness can  
 107 be found in literature. Several experimental studies have in-  
 108 vestigated the impact of porosity on the longitudinal Young's  
 109 modulus.<sup>16–19</sup> As these studies were reduced to axial direc-  
 110 tion, they did not provide any information on the contribu-  
 111 tion of porosity to the anisotropy. A few studies, based on  
 112 experiments or micromechanics models have examined the  
 113 dependence of effective anisotropic stiffness coefficients on  
 114 tissue properties and especially on porosity. Dependence on  
 115 porosity of four elastic moduli of cortical bone assumed to  
 116 be transversally isotropic has been reported in a single ex-  
 117 perimental study.<sup>14</sup> Micromechanics provided comprehensive  
 118 models of effective elastic properties of bone using various  
 119 hypotheses to describe elastic properties of the bone matrix  
 120 and the pore network.<sup>15,20</sup> In particular, Sevostianov *et al.*<sup>15</sup>  
 121 have depicted the effect of porous network on overall stiff-  
 122 ness coefficients of cortical bone assuming an isotropic bone  
 123 matrix and identifying the effect of pore distribution. In the  
 124 related field of composite media with unidirectional pores, a  
 125 similar analysis was performed by Ichitsubo *et al.*<sup>21</sup> with an  
 126 anisotropic matrix.

127 In this study, we report on microcomputed tomography  
 128 ( $\mu\text{CT}$ ) based FDTD simulations whereby the effective elas-  
 129 tic properties are directly computed for individualized porous  
 130 network of 19 cortical bone microstructures reconstructed  
 131 from high resolution synchrotron radiation microtomography  
 132 (SR- $\mu\text{CT}$ ). The bone matrix was modeled as a homogeneous  
 133 anisotropic medium. As the elastic properties of the bone  
 134 matrix were only partially documented in our samples, four  
 135 built-in models were used for each specimen. The computa-  
 136 tional bone model for ultrasonic propagation in bone and the  
 137 basis of the SR- $\mu\text{CT}$ -based FDTD simulations are described  
 138 in Sec. II. In Sec. III the results of the effective elastic prop-

erties are examined as a function of porosity for the different  
 bone models. We close with a discussion of the limitations  
 and potential extension of the current study.

## II. MATERIALS AND METHODS

### A. Samples

In this study we use a subset of 19 samples from a  
 collection of human radii with soft tissue removed and pre-  
 viously assessed by different experimental techniques such  
 as SR- $\mu\text{CT}$  and scanning acoustic microscopy (SAM), which  
 provided accurate data for cortical bone microstructure and  
 estimates of material properties (density, stiffness) that were  
 used to build the cortical bone models developed in the  
 present paper.

Assessment of the microstructure was reported in Ref. 5.  
 Small portions were cut in the postero-lateral zone of the  
 distal radius. The dimensions were typically 10 mm long in  
 the direction parallel to the bone axis and 8 mm long in the  
 circumferential direction. These volumes were imaged by  
 SR- $\mu\text{CT}$ <sup>22</sup> at the European Synchrotron Radiation Facility  
 (ESRF, Grenoble, France). The radiographs [two-  
 dimensional (2D) projections] were recorded on a  $1024$   
 $\times 1024$  charge-coupled device-based 2D detector and the  
 voxel size was set to  $10 \times 10 \times 10\ \mu\text{m}^3$ . From sets of 2D  
 projections under different angles of view, three-dimensional  
 reconstructions of the microstructure were obtained by to-  
 mography algorithm. The amount of mineral was  
 $1082 \pm 16\ \text{mg}/\text{cm}^3$  in the whole collection of samples.

Among the 19 samples considered in this study, 10 were  
 previously studied by scanning acoustic microscopy at  
 50 MHz with a spatial resolution of  $23\ \mu\text{m}$  and a spatial  
 sampling rate of  $20\ \mu\text{m} \times 20\ \mu\text{m}$ .<sup>23</sup> The section adjacent to  
 the samples investigated by SR- $\mu\text{CT}$  was scanned and a  
 mapping of the acoustic impedance was provided. It was  
 shown that the setup resolved Haversian canals larger than  
 $25\ \mu\text{m}$ . As a consequence, these measurements were repre-  
 sentative of the impedance of the bone matrix at a scale of  
 $20\ \mu\text{m}$ . The acoustical impedance averaged over the whole  
 set of specimens was found to be  $8.1 \pm 0.5\ \text{MRa}$ .

### B. Configuration of the simulation

Propagation of transient 1 MHz plane waves in the 3D  
 reconstructed bone microstructures was computed using a  
 FDTD code, SIMSONIC, developed in the laboratory and de-  
 tailed elsewhere,<sup>6,24</sup> which computes a numerical solution to  
 the 3D linear elastic wave propagation. The algorithm is  
 based on Virieux scheme,<sup>25</sup> and uses first-order derivative in  
 space and time.

The code requires the simulation box to be defined as  
 right angle volume. Therefore, parallelepipedic volumes  
 were extracted from the 3D SR- $\mu\text{CT}$  reconstructed volumes  
 (Fig. 1). The volume of the blocks analyzed in simulation  
 with a spatial step of  $20\ \mu\text{m}$  varies from 9 to  $36\ \text{mm}^3$ , de-  
 pending on the thickness of the sample.

A combination of symmetric boundary conditions (tan-  
 gential velocities equal on both sides of the boundary and  
 normal velocities null on the boundary) and/or antisymmetric  
 boundary conditions (tangential velocities null on the bound-

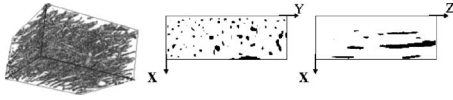


FIG. 1. Three-dimensional porous network (pores are in grey) in a parallel-epipedic block extracted from the  $\mu$ CT reconstructed bone structure. On the right-hand side are shown a transverse and longitudinal cross section through the three-dimensional porous network. The preferential orientation of the pores is along the bone axis.

$$C = \begin{pmatrix} c_{11} & c_{12} & c_{13} & 0 & 0 & 0 \\ c_{12} & c_{22} & c_{23} & 0 & 0 & 0 \\ c_{13} & c_{23} & c_{33} & 0 & 0 & 0 \\ 0 & 0 & 0 & c_{44} & 0 & 0 \\ 0 & 0 & 0 & 0 & c_{55} & 0 \\ 0 & 0 & 0 & 0 & 0 & c_{66} \end{pmatrix} \quad \begin{array}{l} X \leftrightarrow 1 \\ \text{with } Y \leftrightarrow 2, \\ Z \leftrightarrow 3 \end{array} \quad (1)$$

215

where the  $X$  direction corresponds to the radial direction (i.e. thickness direction), the  $Y$  direction is the circumferential direction, and the  $Z$  direction is along the bone axis. But, as described by Katz,<sup>29</sup> the Haversian cortical bone is transverse isotropic in nature because of the locally uniaxial architecture of osteons. Consequently, numerous studies<sup>30–32</sup> assumed the cortical bone as a transverse isotropic elastic solid medium, which reduces the number of independent coefficients of the stiffness matrix to five. Considering transverse isotropy with  $(XY)$  as the isotropic plane,<sup>33–35</sup> the stiffness coefficients of  $C$  verify  $c_{13}=c_{23}$ ,  $c_{22}=c_{11}$ ,  $c_{44}=c_{55}$ , and  $c_{66}=(c_{11}-c_{12})/2$ .

When the waves propagate along principal directions of symmetry, the diagonal terms of the stiffness matrix  $c_{11}$ ,  $c_{12}$ , and  $c_{33}$  are related to the phase velocity of compression-bulk wave which propagates along the  $X$ ,  $Y$ , and  $Z$  direction, respectively, with

$$V_x = \sqrt{\frac{c_{11}}{\rho}}, \quad V_y = \sqrt{\frac{c_{22}}{\rho}}, \quad V_z = \sqrt{\frac{c_{33}}{\rho}}. \quad (2)$$

The stiffness coefficients  $c_{44}$  and  $c_{55}$  are related to the phase velocity of shear wave which propagate in  $Z$  direction and  $c_{66}$  in the transverse plane according to

$$V_{yz} = \sqrt{\frac{c_{44}}{\rho}}, \quad V_{xz} = \sqrt{\frac{c_{55}}{\rho}}, \quad V_{xy} = \sqrt{\frac{c_{66}}{\rho}}. \quad (3)$$

The effective stiffness coefficients were deduced from Eqs. (2) and (3) calculating the effective mass density  $\rho$  with the following rule of mixture:

$$\rho = \rho^0(1-p) + p\rho_w, \quad (4)$$

where  $\rho^0$  is the mass density of the tissue matrix,  $\rho_w$  is the mass density of the fluid filling the pores (water), and  $p$  is the porosity.

#### D. Numerical bone models

Maps of the mass density and of the stiffness coefficients were used as input data in the software. The cortical bone was modeled as a two-phase medium constituted by the bone matrix and the fluid filling the pores. Each phase was supposed to be homogeneous within and between the samples. The spatial variation of density and stiffness in the simulation volume (spatial step of  $20 \mu\text{m}$ ) relies on the presence of the pores. Both components were clearly delineated by segmentation of the original reconstructed SR- $\mu$ CT data and were defined by fixed mass density and stiffness coefficients.

ary and normal velocities equal on both sides of the boundary) on the simulation domain was applied to ensure the propagation of compression and/or shear plane bulk waves. Perfectly matched layers (PML) on sides and edges of the simulation domain were used to avoid unphysical reflections.

SimSonic provides the transient signals associated with transmission of 1 MHz bulk compression or shear waves through the reconstructed volumes. Typical signals are shown in Fig. 2. Plane bulk waves velocities were deduced from time of flight measurements by detection of first signal maximum.

#### C. Derivation of effective stiffness

Effective stiffness coefficients were derived from velocities of simulated pure bulk wave propagating in principal directions and from effective mass density. For cortical bone the general degree of anisotropy is that of orthotropic material symmetry,<sup>27</sup> which is characterized by nine independent stiffness coefficients. The stiffness matrix can be expressed as follows using the abbreviated subscript notation:

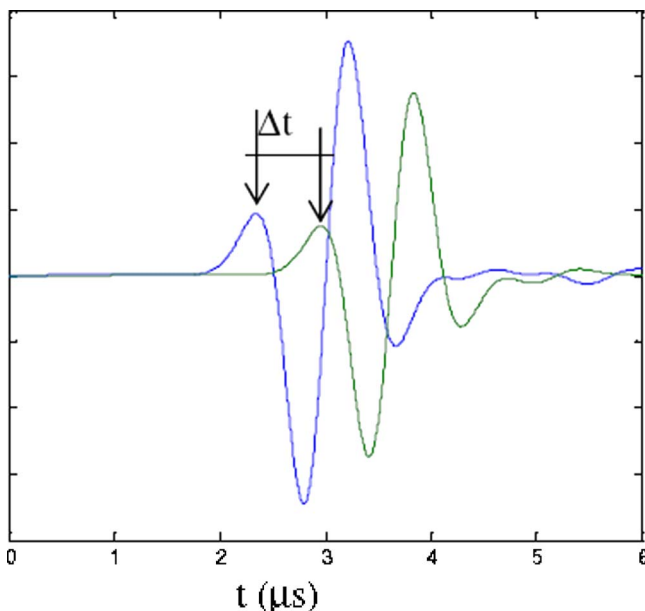


FIG. 2. (Color online) Velocity evaluation from the first maximum signal detection.

TABLE I. Four bone matrix models.

	$c_{33}^0$ (GPa)	$c_{11}^0$ (GPa)	$c_{33}^0/c_{11}^0$	$c_{13}^0/c_{11}^0$	$c_{55}^0/c_{11}^0$	$c_{66}^0/c_{11}^0$
Model 1	34.3	34.3	1	0.43	0.29	0.29
Model 2	34.3	30.6	1.12	0.42	0.34	0.29
Model 3	34.3	27.3	1.26	0.42	0.38	0.31
Model 4	34.3	22.9	1.5	0.41	0.45	0.30

257 Ideal nonviscous fluid (water) was assumed to fill the  
258 pores. The mass density was ( $\rho_f=1 \text{ g/cm}^3$ ), and the stiffness  
259 coefficients were calculated from the following Lamé's con-  
260 stants values ( $\lambda=2.25 \text{ GPa}$ ,  $\mu=0 \text{ GPa}$ ).

261 Simulations in each bone sample microstructure were  
262 conducted with four different models of bone matrix shown  
263 in Table I. For the isotropic case (model 1), two independent  
264 stiffness coefficients are required ( $c_{33}^0$ ,  $c_{13}^0$ ) to define the elas-  
265 ticity of the bone matrix, and in the three transversely isotro-  
266 pic models (models 2–4), five independent stiffness coeffi-  
267 cients are needed ( $c_{11}^0$ ,  $c_{33}^0$ ,  $c_{55}^0$ ,  $c_{13}^0$ , and  $c_{12}^0$ ). Here, the  
268 subscript zero is used to denote the intrinsic stiffness of the  
269 tissue matrix.

270 In all the models, the axial stiffness  $c_{33}^0$  was taken close  
271 to 34 GPa, the overall mass density  $\rho^0$  of the bone matrix  
272 mass  $1.91 \text{ g/cm}^3$ . These values were derived from SR- $\mu$ CT  
273 and SAM data averaged over the samples that were investi-  
274 gated with these techniques. In Ref. 23, the mass density of  
275 the solid matrix was related by a second-order polynomial fit  
276 to the mineral amount. According to this, the mass density in  
277 our study was approximated to a value of  $1.91 \text{ mg/cm}^3$ , con-  
278 sidering the mean value of mineralization previously mea-  
279 sured and neglecting the intersample variations. The axial  
280 stiffness  $c_{33}^0=34.3 \text{ GPa}$  was derived from acoustic imped-  
281 ance ( $Z=8.1 \text{ MRa}$ ) values measured at 50 MHz, with a reso-  
282 lution of  $23 \text{ }\mu\text{m}$  well adapted to spatial grid of the simulation  
283 ( $20 \text{ }\mu\text{m}$ ). The axial stiffness was derived using the relation

$$284 \quad c_{33}^0 = \frac{Z^2}{\rho^0} \quad (5)$$

285 between acoustical impedance and density, with  $\rho^0$   
286  $=1.91 \text{ g/cm}^3$ . Because the standard deviation of the acoustic  
287 impedance over the samples was small and the variations of  
288 the mean value of the acoustic impedance were weak be-  
289 tween the different regions investigated, a fixed value of  $c_{33}^0$   
290 was adopted within and between specimens. We choose to  
291 couple the numerical simulations to experimental data ob-  
292 tained on the same set of specimens investigated by both  
293 scanning acoustic microscopy and  $\mu$ CT. This might have  
294 resulted in stiffness values slightly higher than values re-  
295 ported in the literature.<sup>14,36</sup> We do not expect the trends re-  
296 ported here to be accurate in an absolute sense. However,  
297 since our main conclusion is based on the comparative per-  
298 formance of the models, the general trends reported here are  
299 expected to hold in a relative sense. All four models are built  
300 around the same value of  $c_{33}^0$ . It would be interesting to carry  
301 out a parametric study on the influence of this absolute value.

302 With models 2–4, transversely isotropic bone matrices  
303 with various degrees of anisotropy were explored. The value  
304 of the anisotropy ratio  $AR_0=c_{33}^0/c_{11}^0$  was chosen in the range  
305 1–1.5. The value of  $c_{11}^0$  was therefore determined from the  
306 selected anisotropy ratio value. Moreover, for the three trans-  
307 versely isotropic matrix (models 2–4), the shear stiffness co-  
308 efficient  $c_{55}^0$  was fixed to  $10.4 \text{ GPa}$ .

309 The other stiffness coefficients,  $c_{13}^0$  and  $c_{12}^0$ , were derived  
310 from the relationship between Poisson's ratio and stiffness,  
311 assuming the bone matrix to be either isotropic (model 1) or  
312 transversely isotropic (models 2–4), with the following rela-  
313 tionships:

$$314 \quad \nu_L^0 = \frac{c_{13}^0}{c_{11}^0 + c_{12}^0}, \quad \nu_T^0 = \frac{c_{33}^0 c_{12}^0 - (c_{13}^0)^2}{c_{33}^0 c_{11}^0 - (c_{13}^0)^2}. \quad (6)$$

315 The longitudinal  $\nu_L^0$  and the transverse  $\nu_T^0$  Poisson's ratios  
316 were equal and set to a value of 0.3, a commonly used value  
317 in the literature.<sup>38–40</sup> Model 2 was build with  $AR_0=1.12$ , a  
318 value reported in Hofmann *et al.*<sup>37</sup> In model 3, a ratio of  
319 anisotropy  $c_{33}^0/c_{11}^0=1.26$  was adopted, according to Turner's  
320 report.<sup>38</sup> In addition, we kept in this model the value of the  
321 longitudinal shear modulus given in Ref. 37 providing  $c_{55}^0$ .

322 Model 4 was used to enlarge the range of anisotropy  
323 ratio and  $AR_0$  reaches the value of 1.5, the value of  $c_{33}^0$  and  
324  $c_{55}^0$  remaining the same as in models 2 and 3.

### 325 E. Pore size and porosity

326 Figure 2 shows a typical 3D reconstruction of the porous  
327 network. To perform numerical simulation, the original grey  
328 scale reconstructions were segmented to yield binary map-  
329 pings of the porous network. The segmentation threshold laid  
330 between the two well-separated distributions of pixel values

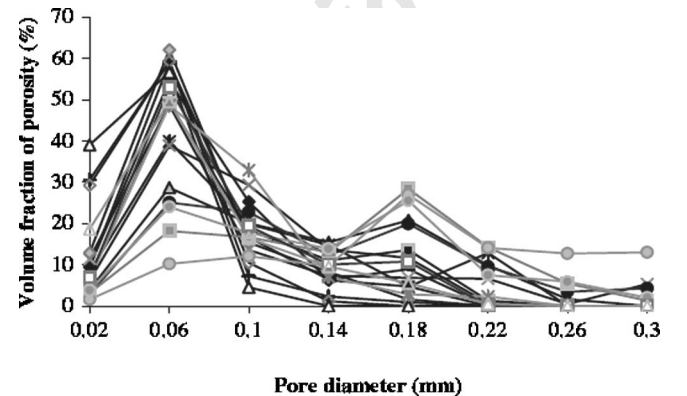


FIG. 3. Distribution of pores diameter through the 19 samples.

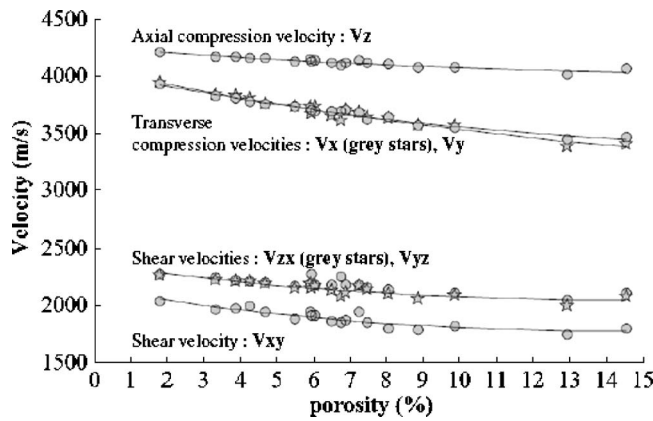


FIG. 4. Effective compression and shear bulk wave velocities deduced from FDTD simulations as a function of cortical porosity (model 2). The grey stars represent  $V_x$  and  $V_{zx}$ .

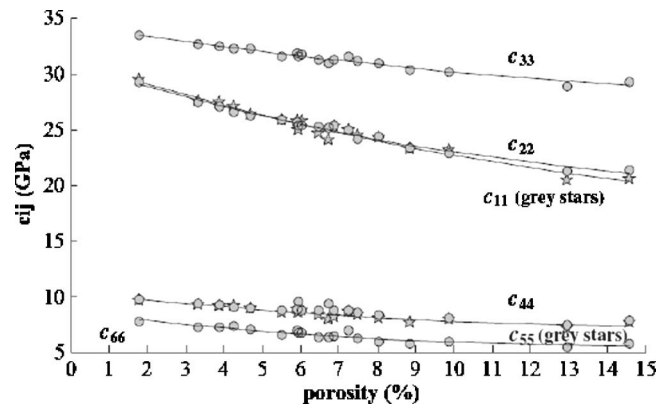


FIG. 5. Effective diagonal stiffness coefficients as a function of porosity (model 2).

331 corresponding to the bone tissue and to the empty pores. The  
 332 porosity was defined for each specimen as the ratio of the  
 333 volume of pores to the total bone volume. The pore area  
 334 related to different pore diameters was estimated in each re-  
 335 constructed tomographic cross section, and then the pore ar-  
 336 eas were summed over the cross sections and multiplied by  
 337 the spatial step increment between two consecutive slices to  
 338 obtain the porosity. The distribution of the porosity as func-  
 339 tion of pore diameters was deduced from the morphological  
 340 analysis of the 19 reconstructed microstructures. In addition,  
 341 structural parameters such as mean pore density (number of  
 342 detected pores per  $\text{mm}^2$ ) and mean pore diameter (the  
 343 equivalent diameter was determined from the area of the in-  
 344 dividual canals) were extracted.

### 345 III. RESULTS

#### 346 A. Pore size and porosity

347 Each of the 19 samples had a porosity falling in the  
 348 range 2%–15%. The distribution of diameters for the 19  
 349 specimens illustrated in Fig. 3 shows a bimodal distribution  
 350 with two pore classes, the 60- and the 180- $\mu\text{m}$ -diam groups,  
 351 as contributors to the porosity (Fig. 3). The spatial resolution  
 352 of SR- $\mu\text{CT}$  was not sufficient to resolve the smallest pores  
 353 (osteocytes lacunae, canaliculi) of a few microns in diameter.  
 354 A higher resolution ( $<10 \mu\text{m}$ ) is needed to consistently vi-  
 355 sualize all cortical pores in human bone.<sup>41</sup>

356 The average porosity in these samples was about 7%,  
 357 the average pore number density was  $15 \text{ mm}^{-2}$ , and the mean

pore diameter was about  $80 \mu\text{m}$ . These results are consistent  
 with previous morphological studies on human cortical  
 bone.<sup>23,42</sup>

#### B. Effective velocities and stiffness coefficients as a function of cortical porosity

Velocities of compression and shear bulk plane waves  
 along the three principal axes of symmetry were computed  
 for the 19 bone specimens and the 4 models. Figure 4 pre-  
 sents results for model 2. All the effective compression and  
 shear bulk wave velocities decrease when porosity increases.  
 However, the decrease was less pronounced for propagation  
 along the long axis of the bone compared to the transverse  
 directions. For a 10% increase in porosity, waves that propa-  
 gate in the transverse plane undergo a decrease of 12%  
 (470 m/s) for compression waves and 17% (370 m/s) for  
 shear waves, while waves that propagate in the Z direction  
 are reduced by 4% (160 m/s) for compression waves and  
 11% (260 m/s) for shear waves.

Similar trends of velocity variation versus porosity were  
 observed for the four bone matrix models (Table II).

As a consequence of the decrease of both the effective  
 mass density [Eq. (4)] and bulk wave velocities (Fig. 4) with  
 the porosity, all the effective diagonal stiffness coefficients  
 decline with the porosity as illustrated for model 2 in Fig. 5.

In all the bone models, a quadratic law between stiffness  
 coefficients and porosity ( $ap^2+bp+c$ ) was a better fit than a  
 linear regression, although the first coefficient of the poly-  
 nomial was small (see Table III).

TABLE II. Absolute (relative variation) of compression and shear waves velocities for a 10% increase of porosity (from 0 to 10%).

(m/s)	Compression waves in the transverse plane $V_x$ and $V_y$	Compression wave in the axial direction $V_z$	Shear wave in the transverse plane $V_{xy}$	Shear waves in the axial direction $V_{zx}$ and $V_{yz}$
Model 1	530 (12%)	190 (4.5%)	380 (17%)	250 (11%)
Model 2	470 (12%)	160 (4%)	370 (17%)	260 (11%)
Model 3	420 (11%)	150 (3.5%)	355 (17%)	200 (9%)
Model 4	350 (10%)	130 (3%)	320 (11%)	270 (11%)

TABLE III. Quadratic law variations of the diagonal stiffness coefficients vs porosity  $c_{ii}=a(p\%)^2+bp\%+c$ .

$AR^0=1.12$	$c_{11}$	$c_{22}$	$c_{33}$	$c_{44}$	$c_{55}$	$c_{66}$
$a$	0.024	0.026	0.011	0.004	0.013	0.014
$b$	-1.088	-1.047	-0.527	-0.232	-0.398	-0.412
$c$	31.15	30.82	34.37	10.14	10.47	80.60
$R^2$	0.97	0.98	0.96	0.80	0.88	0.88

386 **C. Porosity contribution to effective anisotropy**

387 The influence of porosity on effective stiffness is weaker  
 388 in the axial direction (i.e., for  $c_{33}$  and for  $c_{44}$  and  $c_{55}$ ) com-  
 389 pared to the transverse directions (i.e., for  $c_{11}$  and  $c_{22}$  and for  
 390  $c_{66}$ ), a result that contributes to the increase of the effective  
 391 anisotropy as a function of porosity compared to the original  
 392 elastic anisotropy of the bone matrix.

393 The effective anisotropy ratio ( $AR=c_{33}/c_{11}$ ) normalized  
 394 by the intrinsic anisotropy ratio of the bone matrix ( $AR^0$   
 395  $=c_{33}^0/c_{11}^0$ ) is plotted as a function of porosity for the four  
 396 different bone models in Fig. 6. Normalized anisotropy ratios  
 397 are consistently found to be greater than one and increasing  
 398 with the porosity. The data indicate that the porosity contrib-  
 399 utes to the overall effective elastic anisotropy of bone struc-  
 400 ture. The higher the porosity, the higher its contribution to  
 401 the bone elastic anisotropy. A 10% increase of porosity (from  
 402 0 to 10%) results in a relative increase of anisotropy ranging  
 403 between 16% (for  $AR^0=1.5$ ) and 20% (for the isotropic case)  
 404 for the four bone matrix models studied.

405 Furthermore, the effective shear anisotropy ratio ( $AR'$   
 406  $=c_{55}/c_{66}$ ) increases with the porosity: For a 10% increase of  
 407 porosity, the  $AR'$  is 16% greater for the isotropic case  
 408 (model 1), 14% greater for models 2 and 3, and 12% greater  
 409 for model 4.

AQ: #3 410 The relative contribution of porosity to structural aniso-  
 411 tropy of cortical bone is all the more important as the bone  
 412 matrix is weakly anisotropic.

413 On the other hand, the other anisotropy ratios assessed  
 414 by FDTD simulations ( $c_{ii}/c_{11}$ ) were found to remain almost  
 415 unchanged with the porosity.

IV. DISCUSSION

416

Our results suggest that the porous network introduces  
 or reinforces transverse isotropy, as expected owing to its  
 preferential orientation parallel to the bone axis. Indeed, it is  
 noteworthy that the effect of porosity is similar for  $c_{11}$  and  
 $c_{22}$ , and for  $c_{44}$  and  $c_{55}$ . As pictured by Fig. 5, the differences  
 between  $c_{11}$  and  $c_{22}$  and between  $c_{44}$  and  $c_{55}$  induced by the  
 porous network were subtle: for example,  $(c_{11}-c_{22})/c_{11} \leq 2$   
 $\times 10^{-4}$  for  $p \leq 10\%$  and  $(c_{11}-c_{22})/c_{11} \approx 4 \times 10^{-2}$  for  
 $p \geq 10\%$ . Therefore, if either isotropic (model 1) or trans-  
 versely isotropic symmetry (models 2-4) is assumed for the  
 tissue matrix, the introduction in the bone model of the ori-  
 ented porous network resulted in a structure with effective  
 transversely isotropic elastic properties. The result is consis-  
 tent with the well-known effective macroscopic transverse  
 isotropy of human cortical bone.<sup>35,43-45</sup>

However, two additional conditions,  $c_{13}=c_{23}$  and  $c_{66}$   
 $=(c_{11}-c_{12})/2$ , required by this symmetry could not be  
 checked here because mixed-indices stiffness coefficients  
 were not evaluated. The evaluation of the mixed-indices  
 stiffness coefficients  $c_{12}$ ,  $c_{13}$ , and  $c_{23}$  requires one either to  
 rotate the sample or to record angular variation of transmit-  
 ted bulk wave. In the first case, it would be necessary to  
 modify the software to implement capabilities of working  
 with material of more general anisotropy than orthotropy,  
 and in the second case it would be necessary to implement a  
 more sophisticated signal processing. As these tasks were not  
 under the scope of this study, the stiffness coefficients  $c_{12}$ ,  
 $c_{13}$ , and  $c_{23}$  were not evaluated. However, note that under the  
 reasonable assumption of a macroscopic transverse aniso-  
 tropy,  $c_{12}$  can be simply derived from the knowledge of  $c_{11}$   
 and  $c_{66}$  with  $c_{66}=(c_{11}-c_{12})/2$ .

Coupling  $\mu$ CT-based models of bone microstructure  
 with FDTD simulations is a powerful means to compute the  
 effect of porosity on effective stiffness and elastic anisotropy  
 of bone. The high spatial resolution reached by SR- $\mu$ CT al-  
 lows an accurate determination of the porous network. How-  
 ever, the bone computational model also requires input data  
 for the stiffness of the bone tissue matrix. Because the com-  
 plete set of real data (five stiffness coefficients and mass  
 density) for the bone matrix was not known, some hypoth-  
 eses were made. The Poisson's ratios are not easy to deter-  
 mine experimentally and therefore are not known with accu-  
 racy, and an *a priori* value of 0.3 for the Poisson's ratios was  
 assumed, following a commonly adopted assumption in  
 many studies, especially finite element analyses,<sup>46</sup> despite  
 the rather wide range of values, between 0.12 and 0.63, re-  
 ported in literature.<sup>32,43</sup> Thus, one limitation of our study is  
 related to the assumption adopted regarding the values of the

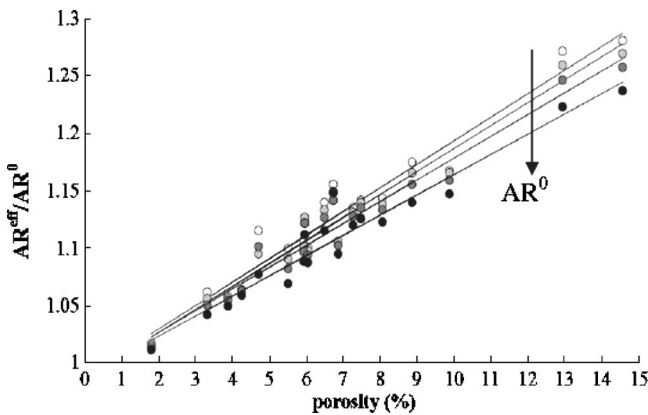


FIG. 6. Normalized effective anisotropy ratio ( $AR/AR_0$ ) as a function of porosity for the different bone matrix models. Open circles correspond to the isotropic case (model 1), the light grey circles to model 2 ( $AR^0=1.12$ ), the dark grey circles to model 3 ( $AR^0=1.26$ ), and the closed circles to model 4 ( $AR^0=1.5$ ).

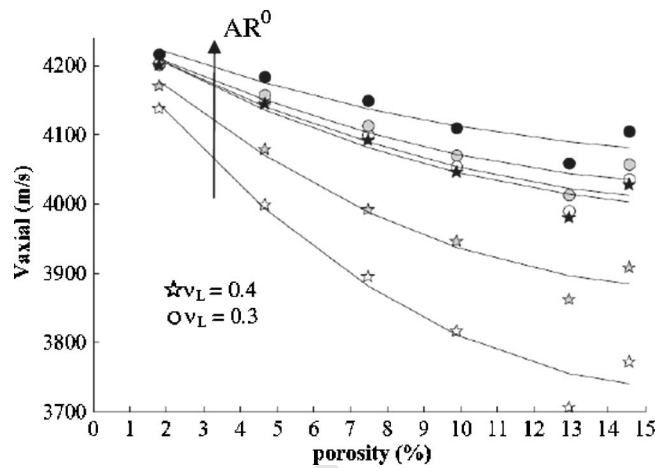


FIG. 7. Influence of the longitudinal Poisson's ratio on the dependence of the axial velocity on the cortical porosity. The stars represent the data obtained for  $\nu_L=0.4$  and the circles represent the data related to  $\nu_L=0.3$ . The colors from white to black correspond to increasing  $AR^0$  (model 1, model 2, and model 4).

465 Poisson's ratios, as mentioned in Raum *et al.*<sup>23</sup> Here, in a  
466 first step we have investigated the influence of the longitudi-  
467 nal Poisson's ratio value on the axial velocity as a function of  
468 porosity for model 1 (model 1 is isotropic, the longitudinal  
469 and transverse Poisson's ratios are equal), model 2, and  
470 model 4. For these bone models, the computations have been  
471 run with an input Poisson's ratio value of 0.4 instead of 0.3.  
472 The new Poisson's ratio value was properly taken into ac-  
473 count by modifying the value of the stiffness coefficients  $c_{12}^0$   
474 and  $c_{13}^0$  according to Eq. (6).

AQ: #4  
475 The influence of the Poisson's ratio value on the axial  
476 velocity is presented in Fig. 7. The increase of Poisson's ratio  
477 from 0.3 to 0.4 induces a stronger impact of porosity on axial  
478 velocity and a better differentiation of the behavior between  
479 the different anisotropy models. For a longitudinal Poisson's  
480 ratio of 0.3 and a 10% increase of porosity, the axial velocity  
481 decreases by 190 m/s (4%) for model 1, 165 m/s (4%) for  
482 model 2, and 130 m/s (3%) for model 4. When the longitu-  
483 dinal Poisson's ratio is fixed to 0.4, the impact of a 10%  
484 increase of porosity on the axial velocity is of 430 m/s  
485 (10%) for model 1, 300 m/s (7%) for model 2, and 200 m/s  
486 (5%) for model 4. Consequently, an accurate estimation of  
487 the Poisson's ratios or of the related stiffness coefficients,  
488 especially the mixed-indices ones, at the matrix level is criti-  
489 cal for a reliable prediction of relative variation of ultrasound  
490 velocities as function of porosity. Advances in this field have  
491 been published recently.<sup>32,46</sup>

492 The present study permits a direct assessment of the  
493 effect of porosity on the stiffness coefficients of cortical  
494 bone. However, the morphology of the porous network is  
495 complex and requires several parameters to be fully charac-  
496 terized, including the size of the pores, pore density (number  
497 of pores per unit of area), spatial distribution of the pores,  
498 and shape of the pores.<sup>47</sup> The question arises as to whether  
499 these properties are determinant factors of the effective stiff-  
500 ness and the elastic anisotropy of cortical bone. Simplified  
501 models of porous networks were numerically built in order to  
502 better understand these effects for fixed values of porosity.

Preliminary results (not shown here) suggest that the influ- 503  
ence of morphological parameters is small. For example, 504  
with a simplified model with a periodic spatial distribution of 505  
cylindrical inclusions embedded in the bone matrix, with 506  
their axis parallel to the axis of the bone, only subtle differ- 507  
ence of 2% in the axial compression velocity could be obser- 508  
ved. However, more work is required to explore the conse- 509  
quences of morphological variations in the cortical 510  
porosity on effective elastic properties. 511

The results of the present study can be used to elaborate 512  
sophisticated macroscopic computational bone models incor- 513  
porating realistic CT-based macroscopic bone structures and 514  
effective elastic properties derived from  $\mu$ CT-based FDTD 515  
simulations taking into account the effect of cortical porosity. 516  
These macroscopic computational bone models are of consi- 517  
derable interest as they can be used in order to evaluate the 518  
effect of porosity and of macroscopic bone structure on mea- 519  
sured velocities in axial transmission. The frequency band- 520  
width (around 1 MHz) in this study is in the range of that 521  
typically used in some of the clinical settings. However, as 522  
mentioned in Sec. I, other devices are working at lower fre- 523  
quencies (around 250 kHz). Work on velocity frequency dis- 524  
persion in cortical bone is sparse. Studying the frequency 525  
dependence of stiffness coefficients is potentially important. 526  
Therefore, specific attention must be paid in future works to 527  
the determination of phase velocity and amplitude in differ- 528  
ent frequency ranges. 529

## V. CONCLUSION 530

The effect of oriented cortical bone porosity on ultra- 531  
sound plane bulk wave velocities and elastic stiffness coef- 532  
ficients was investigated using transient numerical simula- 533  
tion of ultrasound plane bulk waves in 3D reconstructed 534  
microstructure of cortical bone samples. The effective stiff- 535  
ness coefficients were found to decrease with increasing po- 536  
rosity. The preferential orientation of the pore network along 537  
the bone axis induced an additional anisotropy (16%–20%) 538  
of the effective medium compared to the initial anisotropy of 539  
the bone tissue matrix. With initial Poisson's ratios values of 540  
0.3, the variation of the effective anisotropy ratio was found 541  
to be fairly the same whatever the original anisotropy of the 542  
bone matrix was. However, the Poisson's ratio of the elastic 543  
bone matrix was found to be a critical determinant of the 544  
evaluation of relative variation of effective velocities and in 545  
turn of effective stiffness coefficients as a function of poros- 546  
ity. 547

<sup>1</sup>D. Hans, S. K. Srivastav, C. Singal, R. Barkmann, C. F. Njeh, E. Kantoro- 548  
vitch, C. C. Gluer, and H. K. Genant, "Does combining the results from 549  
multiple bone sites measured by a new quantitative ultrasound device 550  
improve discrimination of hip fracture?," *J. Bone Miner. Res.* **14**, 644–651 551  
(1999). 552

<sup>2</sup>P. Moilanen, P. H. F. Nicholson, T. Kärkkäinen, Q. Wang, J. Timonen, and 553  
S. Cheng, "Assessment of the tibia using ultrasonic guided waves in pu- 554  
bertal girls," *Osteoporosis Int.* **14**, 1020–1027 (2003). 555

<sup>3</sup>E. Bossy, M. Talmant, M. Defontaine, F. Patat, and P. Laugier, "Bidirec- 556  
tional axial transmission can improve accuracy and precision of ultrasonic 557  
velocity measurement in cortical bone: A validation on test materials," 558  
*IEEE Trans. Ultrason. Ferroelectr. Freq. Control* **51**, 71–79 (2004). 559

<sup>4</sup>A. Tatarinov, N. Sarvazyan, and A. Sarvazyan, "Use of multiple acoustic 560  
wave modes for assessment of long bones: Model study," *Ultrasonics* **43**, 561  
672–680 (2005). 562

- 563 <sup>5</sup>E. Bossy, M. Talmant, F. Peyrin, L. Akrou, P. Cloetens, and P. Laugier,  
564 "An in vitro study of the ultrasonic axial transmission technique at the  
565 radius: 1-MHz velocity measurements are sensitive to both mineralization  
566 and intracortical porosity," *J. Bone Miner. Res.* **19**, 1548–1556 (2004).  
567 <sup>6</sup>E. Bossy, M. Talmant, and P. Laugier, "Three-dimensional simulations of  
568 ultrasonic axial transmission velocity measurement on cortical bone mod-  
569 els," *J. Acoust. Soc. Am.* **115**, 2314–2324 (2004).
- AQ: 570 <sup>7</sup>F. Lefebvre, Y. Deblock, P. Campistrion, D. Ahite, and J. J. Fabre, "Devel-  
#5 571 opment of a new ultrasonic technique for bone and biomaterials in vitro  
572 characterization," *Journal of Biomechanical Materials Research (Applied*  
573 *Biomaterials)* **63**, 441–446 (2002).  
574 <sup>8</sup>P. H. F. Nicholson, P. Moilanen, T. Kärkkäinen, J. Timonen, and S. Cheng,  
575 "Guided ultrasonic waves in long bone: Modelling, experiment and in  
576 vivo application," *Physiol. Meas* **23**, 755–768 (2002).  
577 <sup>9</sup>P. H. F. Nicholson, P. Moilanen, T. Kärkkäinen, J. Timonen, and S. Cheng,  
578 "Guided ultrasonic waves in long bones: Modelling, experiment and in  
579 vivo application," *Physiol. Meas* **23**, 755–768 (2002).  
580 <sup>10</sup>R. Barkmann, E. Kantorovitch, C. Singal, D. Hans, H. K. Genant, M.  
581 Heller, and C. C. Glüer, "A new method for quantitative ultrasound mea-  
582 surements at multiple skeletal sites: First results of precision and fracture  
583 discrimination," *Journal of Clinical Densitometry* **3**, 1–7 (2000).  
584 <sup>11</sup>K. Raum, I. Leguerney, F. Chandelier, E. Bossy, M. Talmant, A. Saied, F.  
585 Peyrin, and P. Laugier, "Bone microstructure and elastic tissue properties  
586 are reflected in QUS axial transmission measurements," *Ultrasound Med.*  
587 *Biol.* **31**, 1225–1235 (2005).  
588 <sup>12</sup>M. Muller, P. Moilanen, E. Bossy, P. H. F. Nicholson, V. Kilappa, J.  
589 Timonen, M. Talmant, S. Cheng, and P. Laugier, "Comparison of three  
590 ultrasonic axial transmission methods for bone assessment," *Ultrasound*  
591 *Med. Biol.* **31**, 633–642 (2005).  
592 <sup>13</sup>P. Moilanen, V. Kilappa, P. Nicholson, J. Timonen, and S. Cheng, "Thick-  
593 ness sensitivity of ultrasound velocity in long bone phantoms," *Ultrasound*  
594 *Med. Biol.* **30**, 1517–1521 (2004).  
595 <sup>14</sup>X. N. Dong and X. E. Guo, "The dependence of transverse elasticity of  
596 human femoral cortical bone on porosity," *J. Biomech.* **37**, 1281–1287  
597 (2004).  
598 <sup>15</sup>I. Sevostianov and M. Kachanov, "Impact of the porous microstructure on  
599 the overall elastic properties of the osteonal cortical bone," *J. Biomech.*  
600 **33**, 881–888 (2000).  
601 <sup>16</sup>D. R. Carter and W. C. Hayes, "The compressive behaviour of bone as a  
602 two phase porous material," *J. Bone Jt. Surg., Am. Vol.* **59**, 954–962  
603 (1977).  
604 <sup>17</sup>J. D. Currey, "The effect of porosity and mineral content on the Young's  
605 modulus of elasticity of compact bone," *J. Biomech.* **21**, 131–139 (1988).  
606 <sup>18</sup>T. S. Keller, Z. Mao, and D. M. Spengler, "Young's modulus, bending  
607 strength, and tissue physical properties of human compact bone," *J. Or-  
608 thop. Res.* **8**, 592–603 (1990).  
609 <sup>19</sup>S. Bensamoun, J.-M. Gherbezza, J.-F. de Belleval, and M.-C. Ho Ba Tho,  
610 "Transmission scanning acoustic imaging of human cortical bone and re-  
611 lation with the microstructure," *Clin. Biomech. (Los Angel. Calif.)* **19**,  
612 639–647 (2004).  
613 <sup>20</sup>X. N. Dong and X. E. Guo, "Prediction of cortical bone elastic constants  
614 by a two-level micromechanical model using generalized self-consistent  
615 method," *J. Biomech. Eng.* **128**, 309–316 (2006).  
616 <sup>21</sup>T. Ichitsubo, M. Tane, O. Hirotsugu, M. Hirao, T. Ikeda, and H. Nakajima,  
617 "Anisotropic elastic constants of lotus-type porous copper: Measurements  
618 and micromechanics modeling," *Acta Mater.* **50**, 4105–4115 (2002).  
619 <sup>22</sup>M. Salome, F. Peyrin, P. Cloetens, C. Odet, A.-M. Laval-Jeantet, J.  
620 Baruchel, and P. Spanne, "A synchrotron radiation microtomography sys-  
621 tem for the analysis of trabecular bone samples," *Med. Phys.* **26**, 2194–  
622 2204 (1999).  
623 <sup>23</sup>K. Raum, R. O. Cleveland, F. Peyrin, and P. Laugier, "Derivation of elastic  
624 stiffness from site-matched mineral density and acoustic impedance  
625 maps," *Phys. Med. Biol.* **51**, 747–758 (2006).  
626 <sup>24</sup>E. Bossy, F. Padilla, F. Peyrin, and P. Laugier, "Three-dimensional simu-  
627 lation of ultrasound propagation through trabecular bone structures mea-  
628 sured by Synchrotron tomography," *Phys. Med. Biol.* **50**, 5545–5556  
(2005).
- <sup>25</sup>J. Virieux, "P-SV wave propagation in heterogeneous media: Velocity-  
stress finite-difference method," *Geophysics* **51**, 889–901 (1986).  
<sup>26</sup>F. Collino and C. Tsogka, "Application of the PML absorbing layer model  
to the linear elastodynamic problem in anisotropic heterogeneous media,"  
*Geophysics* **66**, 294–307 (2001).  
<sup>27</sup>R. B. Ashman, S. C. Cowin, W. C. Van Burskirk, and J. C. Rice, "A  
continuous wave technique for the measurement of the elastic properties  
of cortical bone," *J. Biomech.* **17**, 349–361 (1984).  
<sup>28</sup>B. A. Auld, *Acoustic Fields and Waves in Solids* (Malabar, FL 1973).  
<sup>29</sup>J. L. Katz and K. Ukraincik, "On the anisotropic elastic properties of  
hydroxyapatite," *J. Biomech.* **4**, 221–227 (1971).  
<sup>30</sup>H. S. Yoon and J. L. Katz, "Ultrasonic wave propagation in human cortical  
bone. II. Measurement of elastic properties and microhardness," *J. Bio-  
mech.* **9**, 459–462 (1976).  
<sup>31</sup>J. L. Katz, "Anisotropy of Young's modulus of bone," *Nature (London)*  
**283**, 106–107 (1980).  
<sup>32</sup>M. Pithioux, P. Lasaygues, and P. Chabrand, "An alternative ultrasonic  
method for measuring the elastic properties of cortical bone," *J. Biomech.*  
**35**, 961–968 (2002).  
<sup>33</sup>W. C. Van Burskirk, S. C. Cowin, and R. N. Ward, "Ultrasonic measure-  
ments of orthotropic elastic constants of bovine femoral bone," *J. Bio-  
mech. Eng.* **103**, 67–71 (1981).  
<sup>34</sup>J. L. Katz, H. S. Yoon, S. Lipson, R. Maharidge, A. Meunier, and P.  
Christel, "The effects of remodeling on the elastic properties of Bone,"  
*Calcif. Tissue Int.* **36**, S31–S36 (1984).  
<sup>35</sup>J. Y. Rho, "An ultrasonic method for measuring the elastic properties of  
human tibial cortical and cancellous bone," *Ultrasonics* **34**, 717–783  
(1996).  
<sup>36</sup>K. Hasegawa, C. H. Turner, and D. B. Burr, "Contribution of collagen and  
mineral to the elastic anisotropy of bone," *Calcif. Tissue Int.* **55**, 381–386  
(1994).  
<sup>37</sup>T. Hofmann, F. Heyroth, H. Meinhard, W. Fränzel, and K. Raum, "Assess-  
ment of composition and anisotropic elastic properties of secondary osteon  
lamellae," *J. Biomech.* **39**, 2282–2294 (2006).  
<sup>38</sup>C. H. Turner, J. Y. Rho, Y. Takano, T. Y. Tsui, and G. M. Pharr, "The  
elastic properties of trabecular and cortical bone tissues are similar: Re-  
sults from two microscopic measurement techniques," *J. Biomech.* **32**,  
437–441 (1999).  
<sup>39</sup>J. Y. Rho, P. Zioupos, J. D. Currey, and G. M. Pharr, "Microstructural  
elasticity and regional heterogeneity in human femoral bone of various age  
examined by nano-indentation," *J. Biomech.* **35**, 189–198 (2002).  
<sup>40</sup>C. E. Hoffer, X. E. Guo, P. K. Zysset, and S. A. Goldstein, "An applica-  
tion of nano-indentation technique to measure bone tissue lamellae prop-  
erties," *J. Biomech. Eng.* **127**, 1046–1053 (2005).  
<sup>41</sup>D. M. L. Cooper, J. R. Matyas, M. A. Katzenberg, and B. Hallgrímsson,  
"Comparison of microcomputed tomographic and microradiographic mea-  
surements of cortical bone porosity," *Calcif. Tissue Int.* **74**, 437–447  
(2004).  
<sup>42</sup>D. M. L. Cooper, A. L. Turinsky, C. W. Sensen, and B. Hallgrímsson,  
"Quantitative 3D analysis of the canal network in cortical bone by micro-  
computed tomography," *Anat. Rec.* **274B**, 169–179 (2003).  
<sup>43</sup>D. T. Reilly and A. H. Burstein, "The elastic and ultimate properties of  
compact bone tissue," *J. Biomech.* **8**, 393–405 (1975).  
<sup>44</sup>A. Ambardar and C. D. Ferris, "Compact anisotropic bone: Elastic con-  
stants, in vitro aging effects and numerical results of a mathematical  
model," *Acta Biol. Acad. Sci. Hung.* **29**, 81–94(1978).  
<sup>45</sup>S. Lipson and J. L. Katz, "The relationship between elastic and micro-  
structure of bovine cortical bone," *J. Biomech.* **17**, 231–240 (1984).  
<sup>46</sup>R. Shahar, P. Zaslansky, A. A. Fiesem, J. D. Currey, and S. Weiner,  
"Anisotropic Poisson's ratio and compression modulus of cortical bone  
determined by speckle interferometry," *J. Biomech.* **40**, 252–264 (2007).  
<sup>47</sup>D. M. L. Cooper, A. L. Turinsky, C. W. Sensen, and B. Hallgrímsson,  
"Effect of voxel size on 3D micro-CT analysis of cortical bone porosity,"  
*Calcified Tissue International* (in press).

629

630

631

632

633

634

635

636

637

638

639

640

641

642

643

644

645

646

647

648

649

650

651

652

653

654

655

656

657

658

659

660

661

662

663

664

665

666

667

668

669

670

671

672

673

674

675

676

677

678

679

680

681

682

683

684

685

686

687

688

689

690

691

692

693

AQ:

#6

AQ:

#7

**AUTHOR QUERIES — 028709JAS**

- #1 AQ: Check renumbering of references.
- #2 AQ: Ok?
- #3 AQ: Check edited sentence
- #4 AQ: Check edited sentence
- #5 Au, pls. supply Issn/coden for Refs. 7 & 10 if possible
- #6 AQ: Supply publisher
- #7 AQ: Please update

PROOF COPY 028709JAS